

Analysis of electron spin echoes by spectral representation of the stochastic Liouville equation^{a)}

Leslie J. Schwartz, Arthur E. Stillman,^{b)} and Jack H. Freed

Baker Laboratory of Chemistry, Cornell University, Ithaca, New York 14853

(Received 4 August 1982; accepted 24 August 1982)

Motional effects can easily be incorporated into calculated spin echo decay envelopes by idealizing the effects of the pulses and by using the stochastic Liouville equation (SLE) to govern the time dependence of the density matrix between pulses. The spectral representation of the 90° - τ - 180° - τ envelope is: $\sum_{l,m} a_{l,m} \exp[-(A_l + A_m^*)\tau]$, where A_l is the l th eigenvalue of the SLE matrix, and $a_{l,m}$ are products of relevant components of eigenvectors. The long time (large τ) phase memory time T_m^∞ is equal to $(\text{Re } A_1)^{-1}$, where A_1 is the smallest eigenvalue. For an axially symmetric g -tensor case in the slow motional region, $T_m^\infty/\tau_R \simeq 3|F\tau_R|^{-1/2}$, $2|F\tau_R|^{-1/3}$, and 1, for Brownian, free, and jump diffusion models, respectively, with $F \equiv 2\beta_e H_0(g_{\parallel} - g_{\perp})/3\hbar$ and τ_R the rotational correlation time. Analogous results hold for nitroxides having nuclear hyperfine tensors. The echo results are compared with simple methods of measuring τ_R from cw spectra. The overall shape of the echo envelopes in the slow motional region is $\exp(-bF^2\tau^3/\tau_R)$ for very short times and $\exp(-2\tau/T_m^\infty)$ for the longer times. Carr-Purcell (CP) sequences suppress the initial exponential in τ^3 and increase the phase memory times as a function of decreasing τ . Detailed analysis of CP sequences can provide information on motional model. The analysis of motional averaging of nuclear modulation effects by our method is also given and it is pointed out that this approach may be useful in studying very slow motions. Despite the simplicity of the methods, we are able to approximately fit experimental data from the Tempone/glycerol-water system in both fast and slow motional regions.

I. INTRODUCTION

Electron spin echo (ESE) spectroscopy is emerging as an important method for studying molecular dynamics in liquids.¹⁻⁶ ESE phase memory times in the slow motional region (i. e., the range of rotational correlation times $\cong 10^{-9}$ to $\cong 10^{-6}$ s) have been shown to be sensitive to the rotational diffusion model^{4,5} and therefore to provide a means to determine the model of diffusion in viscous media. For quantitative studies, computer simulations of the ESE decays must be performed.⁷ These are based on the time-dependent stochastic Liouville formalism developed by Freed and utilized for the interpretation of saturation recovery experiments in liquids.⁸ The great length and complexity of these calculations have motivated us to consider simpler ways of simulating ESE decays. Our present method is based upon the eigenvalues and eigenvectors of the stochastic Liouville equation, which are regularly computed in predicting the cw ESR line shapes.^{9,10} We refer to this method, therefore, as the spectral representation method. We show that in the limit of ideal microwave pulses (i. e., precisely 90° or 180° pulses of infinitesimal duration), this same information is sufficient to predict simple 90° - τ - 180° - τ echo sequences as well as the multipulse Carr-Purcell sequence and its variants.^{11,12}

By means of some prototype examples we can explore typical features of the echo decays in the case of slow motion, and a number of interesting results emerge with regard to their short-time vs long-time behavior and their dependence upon motional model.

We also consider echo modulation envelopes which typically arise from small superhyperfine interac-

tions.^{1,2} We show how the spectral representation method may be successfully applied to study how rotational motion averages out these modulation envelopes. This provides a method to study slower motions than are normally studied by ESE techniques.

In large part, the motivation for this work stems from our preliminary work reported in a recent communication⁵ where the value of studying the eigenvalues of the stochastic Liouville equation is first pointed out.

II. THEORY

Molecules whose rotational degrees of freedom are treated classically as a stationary Markov process and whose spin dynamics are treated quantum mechanically can be characterized by a density matrix $\rho(\Omega, t)$ satisfying the stochastic Liouville equation of motion^{9,9}

$$\frac{\partial}{\partial t} \rho(\Omega, t) = -\hat{\mathcal{H}}^s(\Omega)\rho(\Omega, t) - \Gamma_\Omega[\rho(\Omega, t) - \rho_0(\Omega)], \quad (1)$$

where $\hat{\mathcal{H}}^s(\Omega)$ is the Hamiltonian superoperator of the system [$\hat{\mathcal{H}}(\Omega)$,], depending on the orientation of the molecule specified by its Euler angles Ω . Γ_Ω is the time-independent Markovian operator for the motional process, e. g., a diffusion operator and $\rho_0(\Omega)$ is the equilibrium density matrix.

The Hamiltonian $\hat{\mathcal{H}}(\Omega)$ is divided into three parts

$$\hat{\mathcal{H}}(\Omega) = \hat{\mathcal{H}}_0 + \hat{\mathcal{H}}_1(\Omega) + \hat{\epsilon}(t). \quad (2)$$

The first term $\hat{\mathcal{H}}_0$ is the orientation-independent part of the Hamiltonian in the absence of radiation. For an electron spin interacting with a single nuclear spin

$$\hat{\mathcal{H}}_0 = g_e \beta_e H_0 \hat{S}_z / \hbar - \gamma_n H_0 \hat{I}_z - \gamma_n a \hat{S}_z \hat{I}_z, \quad (3)$$

where g_e and a are the isotropic parts of the electronic g tensor and the nuclear hyperfine tensor, respectively, and H_0 is the applied field. The nuclear g tensor will

^{a)}Supported by NSF Grant No. CHE8024124.

^{b)}Present address: The University of Chicago, Pritzler School of Medicine, Chicago, Ill.

be assumed isotropic.

The orientation-dependent part of the Hamiltonian $\hat{\mathcal{H}}_1(\Omega)$ can be written as a function of the random variable Ω ,

$$\hat{\mathcal{H}}_1(\Omega) = \sum_{m, m'} \mathcal{D}_{-m, m}^2(\Omega) (F_g^{(2, m)} A_g^{(2, m')} + F_A^{(2, m)} F_A^{(2, m')}) , \quad (4)$$

where $\mathcal{D}_{-m, m}^2(\Omega)$ are the Wigner rotation coefficients which transform from the instantaneous orientation of the molecular (unprimed) frame to the fixed (primed) lab frame and $F_g^{(2, m)}$, $F_A^{(2, m')}$ are irreducible components of the electronic g tensor and the nuclear hyperfine tensor, respectively, both written in the molecular frame. In the high field limit, $A_g^{(2, m')}$ is a function of \hat{S}_x , and $F_A^{(2, m')}$ is a function of the products of \hat{S}_x with \hat{I}_x , \hat{I}_y , and \hat{I}_z , all quantized with respect to the lab frame.

In the presence of a rotating field, the Hamiltonian includes the radiation term

$$\hat{\epsilon}(t) = \frac{1}{2} \gamma_e H_1 [\hat{S}_+ \exp(-i\omega t) + \hat{S}_- \exp(i\omega t)] , \quad (5)$$

where H_1 is the magnitude of the rotating microwave radiation and \hat{S}_+ and \hat{S}_- are the electron spin raising and lowering operators.

The Markov operator Γ_Ω has associated with it the equation

$$\frac{\partial}{\partial t} P(\Omega, t) = -\Gamma_\Omega P(\Omega, t) , \quad (6)$$

where $P(\Omega, t)$ is the probability of finding the molecule described by the Euler angles Ω at time t . The equilibrium probability distribution $P_{\text{eq}}(\Omega)$ obeys $\Gamma_\Omega P_{\text{eq}}(\Omega) = 0$.

The equilibrium density matrix $\rho_0(\Omega)$ may be written in the high-temperature approximation as

$$\rho_0(\Omega) \cong \frac{1}{N} (1 - \hbar [\hat{\mathcal{H}}_0 + \hat{\mathcal{H}}_1(\Omega)] / kT) , \quad (7)$$

with N the total number of spin eigenstates. Since we are also considering the high-field limit [for which the form of Eq. (1) is correct^{8,9}], we can keep just $\hat{\mathcal{H}}_0$ in Eq. (7).

We now introduce the reduced density matrix

$$\chi(\Omega, t) \equiv \rho(\Omega, t) - \rho_0(\Omega) \quad (8)$$

and rewrite Eq. (1) as

$$\begin{aligned} \frac{\partial}{\partial t} \chi(\Omega, t) &= (-i\hat{\mathcal{H}}_0^x(\Omega) - \Gamma_\Omega) \chi(\Omega, t) - i\hat{\mathcal{H}}_1^x(\Omega) \rho_0(\Omega) \\ &\equiv -A \chi(\Omega, t) + iq[\hat{\epsilon}(t), \hat{\mathcal{H}}_0] , \end{aligned} \quad (9)$$

where A is the stochastic Liouville operator $q = \hbar / NkT$ and we have used Eq. (7) in its high-field form in the second equality.

Because of the explicit time dependence of $\hat{\epsilon}(t)$ in Eq. (9), we Fourier analyze $\chi(\Omega, t)$ according to

$$\chi(\Omega, t) = \sum_{n=-\infty}^{\infty} \exp(in\omega t) \chi^{(n)}(\Omega, t) , \quad (10)$$

where $\chi^{(n)}(\Omega, t)$ is the n th Fourier component. In the high-field limit, only the $n=0$ component of the diagonal (and pseudodiagonal) density matrix elements and the

$n=1$ component of the density matrix elements off diagonal with respect to the electron spin state enter into the problem.¹³ The components of these off-diagonal elements we write as $Z_\lambda^{(1)}(\Omega, t)$ or simply $Z_\lambda(\Omega, t)$, corresponding to the λ th allowed or forbidden ESR transition. The $Z_\lambda(\Omega, t)$ may be appropriately thought of as the components of these density matrix elements in the frame rotating with the magnetic field. The diagonal density matrix elements for $n=0$ are written simply as $\chi_i^{(0)}(\Omega, t)$. They do not rotate with the field. Finally, we define $\chi_{\text{rf}}^{(n)}(\Omega, t) \equiv \rho_{\text{rf}}(\Omega, t) - \rho_0(\Omega)$ to collectively include only these high field $Z_\lambda^{(1)}(\Omega, t)$ and $\chi_i^{(0)}(\Omega, t)$ density matrix components.

The general approach for solving the operator differential equation, Eq. (9) [with Eq. (10)], is discussed by Freed⁸ and by Stillman and Schwartz.⁷ In order to accurately describe the evolution of the density matrix during some arbitrary pulse sequence,⁷ one first divides the sequence into time regions where a pulse is present and regions where there is no pulse. Equation (9) is then solved in the individual regions. This requires somewhat lengthy and complex calculations, which tend to limit it to only the simplest cases. We therefore adopt an easier approach, based on treating the pulses in an idealized way. We assume that the radiation field is intense and short enough so that the sole effect of a pulse is a rotation of the density matrix by an appropriate angle. Thus, we assume that $\hat{\epsilon}(t)$ dominates the spin-Hamiltonian in the rotating frame [i.e., written in terms of the $Z_\lambda^{(1)}(\Omega, t)$], and more generally, it dominates the stochastic Liouville operator A during this infinitesimal time.

Then, in the absence of any microwave radiation, Eq. (9) [with Eq. (10)] may be written

$$\frac{\partial}{\partial t} \chi_{\text{rf}}^{(n)}(\Omega, t) = -[A_{\text{rf}}^{(n)} \chi_{\text{rf}}^{(n)}(\Omega, t)] , \quad (11)$$

where $A_{\text{rf}}^{(n)} \equiv -i[(\hat{\mathcal{H}}_0 - n\omega \hat{S}_z)^x + \hat{\mathcal{H}}_1(\Omega)^x] - \Gamma_\Omega$, the rotating frame stochastic Liouville operator. The solution to Eq. (11) is

$$\chi_{\text{rf}}^{(n)}(\Omega, t + \tau) = \exp(-A_{\text{rf}}^{(n)} \tau) \chi_{\text{rf}}^{(n)}(\Omega, t) . \quad (12)$$

In the presence of the very intense microwave pulse of short duration we have

$$\begin{aligned} A_{\text{rf}}^{(n)} &= -i[\hat{\mathcal{H}}_0 - n\omega \hat{S}_z]^x + \hat{\mathcal{H}}_1(\Omega)^x + \hat{\epsilon}_{\text{rf}}^x(t)] - \Gamma_\Omega \\ &\cong -i\hat{\epsilon}_{\text{rf}}^x(t) , \end{aligned} \quad (13)$$

where $\hat{\epsilon}_{\text{rf}}^x(t) = \gamma_e H_1 \hat{S}_x / \hbar$. It is here most convenient to return to Eq. (1), which becomes in this limit

$$\frac{\partial}{\partial t} \rho_{\text{rf}}(\Omega, t) \cong -i\hat{\epsilon}_{\text{rf}}^x \rho_{\text{rf}}(\Omega, t) , \quad (14)$$

with the solution

$$\rho_{\text{rf}}(\Omega, t + \tau) = \exp(-i\hat{\epsilon}_{\text{rf}}^x \tau) \rho_{\text{rf}}(\Omega, t) , \quad (15)$$

corresponding to a rotation of the density matrix that only affects the electron spins. Equation (15) is the usual transformation used to describe idealized pulses in earlier analyses of spin echoes that do not include motional modulation in a stochastic Liouville operator.

The effects of this rotation can be calculated by ex-

panding a 2×2 density matrix (whose four elements represent the two electron spin states) in the four Pauli spin matrices and setting

$$\rho(t + \epsilon) = \exp(i\theta \hat{S}_j / \hbar) \rho(t) \exp(-i\theta \hat{S}_j / \hbar)$$

for a rotation by angle $\theta = \gamma_e H_1 t$ about the j th axis.

For rotations about the x axis

$$\rho_{+-}(t + \epsilon) = \frac{-i \sin \theta}{2} [\rho_{+-}(t) - \rho_{-+}(t)] + \left(\cos^2 \frac{\theta}{2} \right) \rho_{+-}(t) + \left(\sin^2 \frac{\theta}{2} \right) \rho_{-+}(t), \quad (16a)$$

$$\rho_{-+}(t + \epsilon) = \rho_{+-}^*(t + \epsilon), \quad (16b)$$

$$\rho_{++}(t + \epsilon) = \frac{-i \sin \theta}{2} [\rho_{++}(t) - \rho_{--}(t)] + \left(\cos^2 \frac{\theta}{2} \right) \rho_{++}(t) + \left(\sin^2 \frac{\theta}{2} \right) \rho_{--}(t), \quad (16c)$$

$$\rho_{--}(t + \epsilon) = \frac{+i \sin \theta}{2} [\rho_{--}(t) - \rho_{++}(t)] + \left(\cos^2 \frac{\theta}{2} \right) \rho_{--}(t) + \left(\sin^2 \frac{\theta}{2} \right) \rho_{++}(t), \quad (16d)$$

where we have only displayed the density matrix element with respect to electron spin. The nuclear-spin part of the matrix element is unchanged by the rotation.

For rotations about the y axis

$$\rho_{+-}(t + \epsilon) = \frac{-\sin \theta}{2} [\rho_{+-}(t) - \rho_{-+}(t)] + \left(\cos^2 \frac{\theta}{2} \right) \rho_{+-}(t) - \left(\sin^2 \frac{\theta}{2} \right) \rho_{-+}(t), \quad (17a)$$

$$\rho_{-+}(t + \epsilon) = \rho_{+-}^*(t + \epsilon), \quad (17b)$$

$$\rho_{++}(t + \epsilon) = \frac{-\sin \theta}{2} [\rho_{++}(t) + \rho_{--}(t)] + \left(\cos^2 \frac{\theta}{2} \right) \rho_{++}(t) + \left(\sin^2 \frac{\theta}{2} \right) \rho_{--}(t), \quad (17c)$$

$$\rho_{--}(t + \epsilon) = \frac{-\sin \theta}{2} [\rho_{--}(t) + \rho_{++}(t)] + \left(\cos^2 \frac{\theta}{2} \right) \rho_{--}(t) + \left(\sin^2 \frac{\theta}{2} \right) \rho_{++}(t). \quad (17d)$$

The observed ESR signal from the λ th transition $S_\lambda(t)$ may be expressed as

$$S_\lambda(t) = \overline{S_\lambda(\Omega, t)} \equiv \int P_{\text{eq}}(\Omega) S(\Omega, t) d\Omega \propto \text{Im} Z_\lambda^{(1)}(\Omega, t), \quad (18)$$

where $S_\lambda(\Omega)$ is the signal from those molecules at an orientation Ω from the λ th transition and the superbar implies averaging over an equilibrium distribution in Ω . Requirement of the imaginary part of $Z_\lambda^{(1)}(\Omega, t)$ is a consequence of the convention of irradiating along the rotating x axis and observing along the y axis. We therefore need to solve for the off-diagonal density matrix elements only.

The $90^\circ - \tau - 180^\circ - \tau$ pulse sequence is particularly simple because the magnetization created in the x - y plane

by the 90° pulse always remains in this plane, i. e., we never interchange components of the diagonal $[\chi_i^{(0)}(\Omega, t)]$ and off-diagonal $[Z_\lambda^{(1)}(\Omega, t)]$ elements of the density matrix. Therefore, we can set up our equations to follow just the time dependence of the components of the off-diagonal elements, which we order in a vector \mathbf{Z} .

At $t = 0$, $\mathbf{Z} = \mathbf{0}$. A $\pi/2$ pulse creates nonzero values for all the components representing allowed electron spin transitions [cf. Eq. (16a)]. The \mathbf{Z} vector just after the 90° pulse $\mathbf{Z}_{\tau/2}(\Omega, 0)$, then evolves for a time τ according to Eq. (12), resulting in a new vector at time τ ,

$$\mathbf{Z}(\Omega, \tau) = \exp(-A_{\tau\tau}) \mathbf{Z}_{\tau/2}(\Omega, 0), \quad (19)$$

where we have dropped the superscript $n = 1$ on $A_{\tau\tau}$. Equation (19) yields the free induction decay following the 90° pulse, and its Fourier transform is just the cw ESR spectrum.

A 180° pulse transforms Eq. (19) into its complex conjugate [cf. Eq. (16a)]

$$\mathbf{Z}_\tau(\Omega, \tau) = \exp(-A_{\tau\tau}^*) \mathbf{Z}_{\tau/2}^*(\Omega, 0). \quad (20)$$

[More precisely, $A_{\tau\tau}^*$ means the complex conjugate of all operators linear in the components of \hat{S} , while those operators independent of \hat{S} (such as the nuclear Zeeman term) are unaffected.]

After another time τ ,

$$\mathbf{Z}(\Omega, 2\tau) = \exp(-A_{\tau\tau}) \exp(-A_{\tau\tau}^*) \mathbf{Z}_{\tau/2}^*(\Omega, 0). \quad (21)$$

Equation (21) is the basic equation representing the $90^\circ - \tau - 180^\circ - \tau$ pulse sequence. The reasoning thus far is easily extended to Carr-Purcell sequences, i. e., sequences represented as $90^\circ - \tau - 180^\circ - 2\tau - 180^\circ - 2\tau - \dots - (180^\circ - 2\tau) - \dots$, with the result

$$\mathbf{Z}(\Omega, n\tau) = \exp(-A_{\tau\tau}) \exp(-A_{\tau\tau}^*) \mathbf{Z}_{\tau/2}^*(\Omega, (n-2)\tau). \quad (22)$$

Pulse sequences which involve other than 180° pulses following an initial 90° pulse may be analyzed in an analogous fashion. However, components of the diagonal density matrix elements $\chi_i^{(0)}(\Omega, t)$, as well as the $Z_\lambda^{(1)}(\Omega, t)$, must be included in the calculation, although Eq. (18) shows that only the off-diagonal elements are detected at the end. General formulas are more cumbersome to write down, because the effects of the pulses [see Eq. (16)] can be to add or switch around elements of $\rho(\Omega, t)$. There is nothing conceptually different about these pulse sequence calculations, however, and we are currently implementing them on the computer.

To proceed further, we expand each $Z_\lambda^{(1)}(\Omega, t)$ in a complete orthonormal set of functions $G_m(\Omega)$,

$$Z_\lambda^{(1)}(\Omega, t) = \sum_{m=1}^{m_{\text{max}}} [C_m(t)]_\lambda G_m(\Omega). \quad (23)$$

It is convenient to choose the $G_m(\Omega)$ as the eigenfunctions of the diffusion operator governing the rotational motion. These are usually the generalized spherical harmonics (or Wigner rotation matrices), the $\mathcal{D}_{KM}^L(\Omega)$. Then, under isotropic conditions [where $P_{\text{eq}}(\Omega)$ is a constant], it can be shown that

$$S(t) \propto \text{Im} \sum_\lambda [C_\lambda(t)]_\lambda, \quad (24)$$

where $[C_0(t)]_\lambda$ is the coefficient in Eq. (23) of \mathcal{D}_{00}^0 . (A similar expression may be written for anisotropic media.⁹)

The vector of expansion coefficients $\mathbf{C}(t)$ is of dimension $\lambda \times m_{\max}$. It follows from Eq. (11) that in the absence of radiation $\mathbf{C}(t)$ obeys the matrix differential equation:

$$\frac{\partial \mathbf{C}(t)}{\partial t} = -B \mathbf{C}(t), \quad (25)$$

where the matrix B is readily obtained from A_{rr} and Eq. (23). The form equivalent to Eq. (12) is

$$\mathbf{C}(t) = \exp(-Bt) \mathbf{C}(0). \quad (26)$$

Equations (13)–(17), which describe the effect of the ideal pulses, can also be cast into such forms. In particular, $\mathbf{Z}_{r/2}(\Omega, 0)$ becomes a new vector in the space spanned by $\mathbf{C}(t)$, which we write as the vector \mathbf{U} (to correspond with previous notation⁸). A 180° pulse takes $\mathbf{C}(t)$ to $\mathbf{C}^*(t)$, (except for the effect on terms in A_{rr} independent of \hat{S} , see above). Therefore, after a 90° - τ - 180° - τ pulse sequence

$$\mathbf{C}(2\tau) = \exp(-B\tau) \exp(-B^*\tau) \mathbf{U}^* \quad (27)$$

and the averaged signal may be written

$$s(2\tau) \propto \text{Re} \{ \mathbf{U}^{\text{tr}} \exp(-B\tau) \exp(-B^*\tau) \mathbf{U}^* \} \quad (28)$$

[the real part is needed because \mathbf{U}^{tr} is pure imaginary, cf. Eqs. (16) and (24)].

Equation (28) can be conveniently computed by introducing the complex orthogonal matrix O which diagonalizes B according to:

$$O^{-1} B O = \Lambda, \quad (29)$$

with Λ a diagonal matrix of eigenvalues Λ_i and $O^{-1} = O^{\text{tr}}$. Equation (28) becomes

$$s(2\tau) \propto \text{Re} \{ \mathbf{U}^{\text{tr}} O \exp(-\Lambda\tau) O^{\text{tr}} O^* \exp(-\Lambda^*\tau) O^{\text{tr}} \mathbf{U}^* \}, \quad (30)$$

In terms of matrix elements, this matrix equation becomes

$$s(2\tau) \propto \text{Re} \sum_{i, j, k, l, m} U_k O_{ki} O_{il} O_{ij}^* O_{mj}^* U_m^* \exp(-[\Lambda_i + \Lambda_j^*]\tau), \quad (31)$$

$$\equiv \text{Re} \sum_{j, l} a_{jl} \exp(-[\Lambda_j + \Lambda_l^*]\tau). \quad (32)$$

Equation (32) expresses the echo as a sum of exponentials of complex argument. This is what we refer to as the spectral representation of the echo. The complex eigenvalues Λ_i and the associated eigenvector components $\sum_k O_{ki} U_k$ determine the cw spectrum as a superposition of complex Lorentzians with width = $\text{Re} \Lambda_i$ and position = $\text{Im} \Lambda_i$. Equation (32) shows how the echo samples the eigenvalue spectrum of the stochastic Liouville operator in a different manner than does either the cw or FID experiment. In particular, the argument of the exponential $(\Lambda_j + \Lambda_l^*)\tau$ leads to the addition of the decaying real parts of these eigenvalues but to the difference of their imaginary parts, which can lead to oscillating beats in the echo envelope.

In the fast motional region, only $2I + 1$ eigenvalues

are important (i.e., small), where I is the nuclear spin. Equations (31) and (32) then predict an echo envelope governed by $2I + 1$ decay constants, Λ_{m_l} , with $T_{2, m_l} = (\text{Re} \Lambda_{m_l})^{-1}$. For very slow motion, the real parts of all the eigenvalues become very small, so that $B = \text{Re} B + i \text{Im} B \cong i \text{Im} B$ and $\exp(-B\tau) \exp(-B^*\tau) \cong 1$. Then, $T_m \rightarrow \infty$.

Finally, we can introduce a physical simplification into Eq. (32) by restricting the summations over l and j to include only those spectral components which are strongly irradiated by the two pulses, i.e., we retain only those eigenvalues Λ_i which satisfy the approximate resonance condition

$$|\omega - \text{Im} \Lambda_i| \leq \gamma_e H_1$$

and denote the restricted summation with a "prime":

$$s(2\tau) \propto \text{Re} \sum_{j, l} a_{jl} \exp(-[\Lambda_j + \Lambda_l^*]\tau). \quad (33)$$

The Carr-Purcell analog to Eq. (33) is

$$s(n\tau) \propto \text{Re} \sum_{i, k, m} \sum_{j, l} U_k O_{ki} O_{il} O_{ij}^* O_{mj}^* \times C_m^*([n-2]\tau) \exp(-[\Lambda_i + \Lambda_j^*]\tau) \quad (34)$$

or

$$|s(n\tau)| \propto \text{Re} \sum_{k, m} U_k \left\{ \sum_i \sum_{j, l} O_{ki} O_{il} O_{ij}^* O_{mj}^* \times \exp(-[\Lambda_i + \Lambda_j^*]\tau) \right\}^n U_m^*. \quad (35)$$

These last equations show how spectral representation can be conveniently used even for multipulse sequences such as Carr-Purcell.

III. EXAMPLES

A. Axially symmetric g tensor

1. 90° - τ - 180° - τ echoes

This is the simplest case for examining electron-spin echoes and slow tumbling with only a single ESR transition. $U_j \propto i\delta_{j,1}$ and Eqs. (31) and (33) simplify to

$$s(2\tau) \propto \text{Re} \sum_{j, l} a_{jl} \exp(-[\Lambda_j + \Lambda_l^*]\tau), \quad (36)$$

$$a_{jl} = \sum_i O_{1i} O_{ij}^* O_{il} O_{ij}^*, \quad (37)$$

where the prime on the summation over j and l has been omitted since we are assuming that the entire spectrum is affected by the pulses.

Figure 1 shows the echo envelope generated by our method for the case where the correlation time $\tau_R = 1 \times 10^{-6}$ s. It has been plotted and fit to a single exponential $\exp(-2\tau/T_M)$ using a linear least squares procedure over two τ ranges: $250 \text{ ns} < \tau < 8 \mu\text{s}$ (gives $T_M = 8.1 \times 10^{-7}$ s) and $250 \text{ ns} < \tau < 1 \mu\text{s}$ (gives $T_M = 5.9 \times 10^{-7}$ s). The figure illustrates the important differences between the long and short time behavior of echo decays, as expected from the form of Eq. (36).

We next compare our results using ideal pulses with

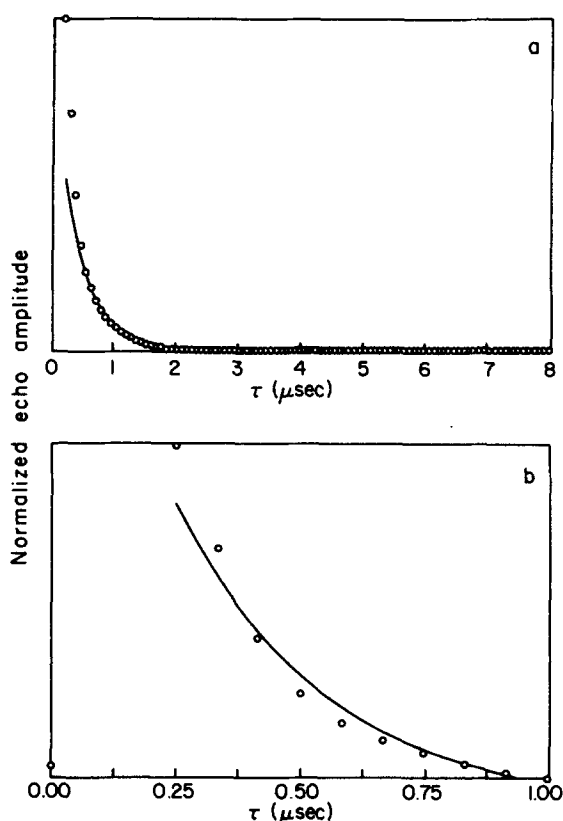


FIG. 1. A typical axially symmetric g -tensor echo envelope, Brownian diffusion, $(g_{\parallel} - g_{\perp}) = -7.5 \times 10^{-4}$, $\tau_R = 1.0 \times 10^{-6}$ s, $|\mathcal{F}| \tau_R = 15$ ($\mathcal{F} = 2\beta_e H_0 (g_{\parallel} - g_{\perp}) / 3\hbar$). Circles—calculated points, solid lines—best least squares fit to $\exp(-2\tau/T_M)$: (a) $T_M = 8.1 \times 10^{-7}$ s; (b) $T_M = 5.9 \times 10^{-7}$ s.

more complete results obtained by Stillman and Schwartz⁷ based on explicit use of the full stochastic Liouville operator during irradiation with a large but finite microwave field applied over a finite time period. In those calculations, each echo envelope was calculated as a function of τ for $\tau > 200$ ns (to mimic usual experimental restrictions) and then fit to the form $\exp(-2\tau/T_M)$. The range of τ fit to each exponential was chosen large enough that an increase in the range did not change the resulting T_M . Since only the simulations for the shorter correlation times ($\tau_R \lesssim 5 \times 10^{-6}$ s) produce an exponential decay (for $\tau > 200$ ns), this procedure (hereafter called the asymptotic T_M^{∞} procedure) effectively selects out only the slowest decaying exponential contributions to the overall echo envelope for the slower motional cases [similar to the T_M result in Fig. 1(a)].

Figure 2 shows log-log plots of T_M^{∞} vs τ_R for the simpler and the more complete theories.⁷ The pulse width assumed in the latter calculation is 5 G, compared to a cw spectrum of ~ 3 G in extent (see Fig. 4), so that the duration of a 90° pulse is 1.8×10^{-6} s, compared to the minimum calculated T_M^{∞} of $\sim 3 \times 10^{-7}$ s. Both calculations assume isotropic reorientation.

The two methods agree perfectly in the fast motional region (i.e., the τ_R range where T_M decreases as τ_R increases). The τ_R dependence in the slow motional region (the τ_R range where T_M increases as τ_R increases) is diffusion model dependent. Shown in Fig. 2 are results using the Brownian model (molecules reorient by random jumps of infinitesimal angle with an infinitesimal time between jumps; $\tau_R = (6R)^{-1}$, where R is the rota-

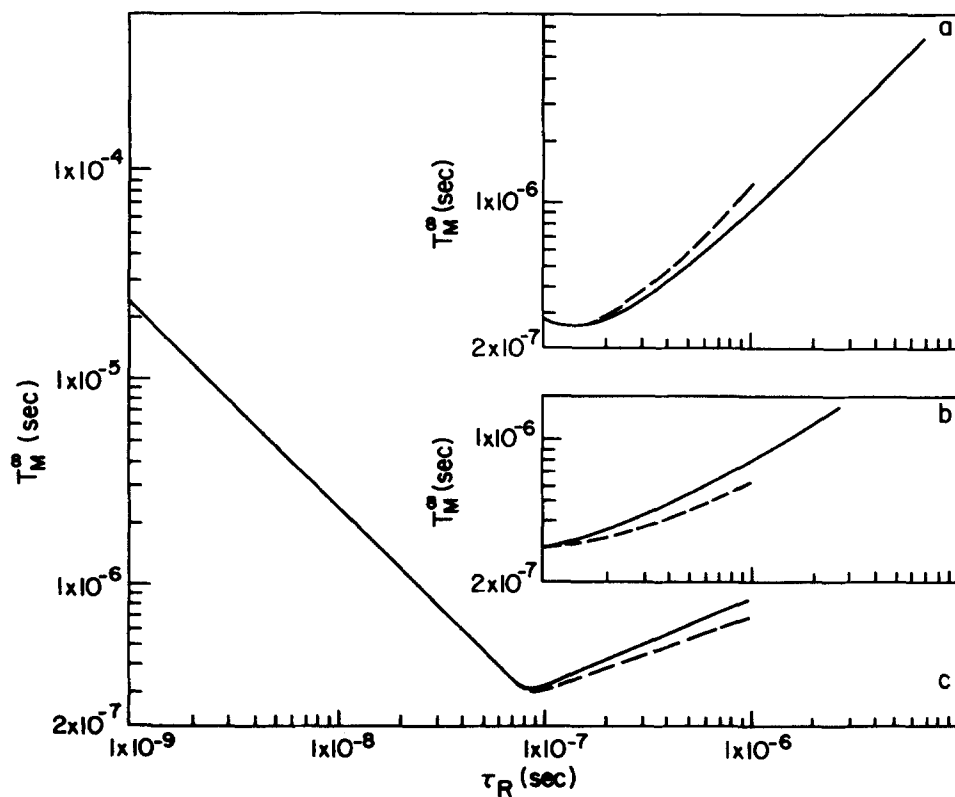


FIG. 2. Comparison of asymptotic phase memory times T_M^{∞} , calculated from the present method (solid lines) and from the more complete method of Stillman and Schwartz (Ref. 7) (dashed lines) incorporating a finite pulse magnitude of 5 G. For large τ_R , T_M^{∞} (present method) can be fit to $T_M^{\infty} \propto \tau_R^b$ ($g_{\parallel} - g_{\perp}) = -7.5 \times 10^{-4}$: (a) jump diffusion, $Rt = 1.0$, $b \approx 0.96$; (b) free diffusion, $Rt = 1.0$, $b \approx 0.63$; (c) Brownian diffusion, $b \approx 0.43$.

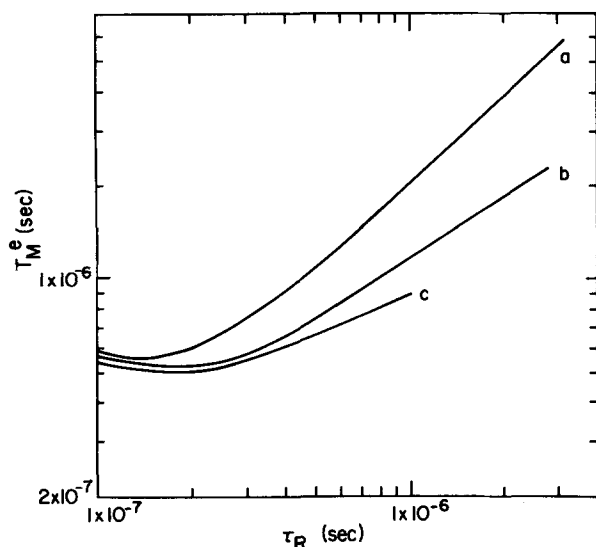


FIG. 3. Phase memory times T_M^e , the time it takes for the echo amplitude to decay to e^{-1} of its value at $\tau = 200$ ns. For large τ_R , T_M^e can be fit to $T_M^e \propto \tau_R^b$. ($g_{\parallel} - g_{\perp} = -7.5 \times 10^{-4}$): (a) jump diffusion, $Rt = 1.0$, $b \approx 0.92$; (b) free diffusion, $Rt = 1.0$, $b \approx 0.63$; (c) Brownian diffusion, $b \approx 0.34$.

tional diffusion constant), the approximate free diffusion model (molecules rotate freely at some orientation for a time t and then instantaneously reorient; $\tau_R = (1 + 6Rt)^{1/2}/6R$), and the jump diffusion model (molecules have random fixed orientations for a time t and then instantaneously reorient; $\tau_R = (1 + 6Rt)/6R$). For the latter two models, Rt was set = 1.0.

We are at present not certain whether the small differences observed between the two methods for slow motion are due to differences in computational method (Stillman and Schwartz⁷ numerically integrated the stochastic Liouville equation with respect to time vs the present use of spectral representation or eigenvalue expansions), or to actual effects from the finite microwave fields of finite duration, although we suspect the latter.

We note that the T_M^e values that we calculate from our method are virtually identical, for each τ_R , to the inverse of the real part of the smallest eigenvalue of B , $(\text{Re } \Lambda_1)^{-1}$. Thus, as expected, Eq. (36) does indeed reduce to a single exponential when measured over a long enough τ range.⁵ We have used this fact to extend the T_M^e curve for the jump model in Fig. 2(a) by simply

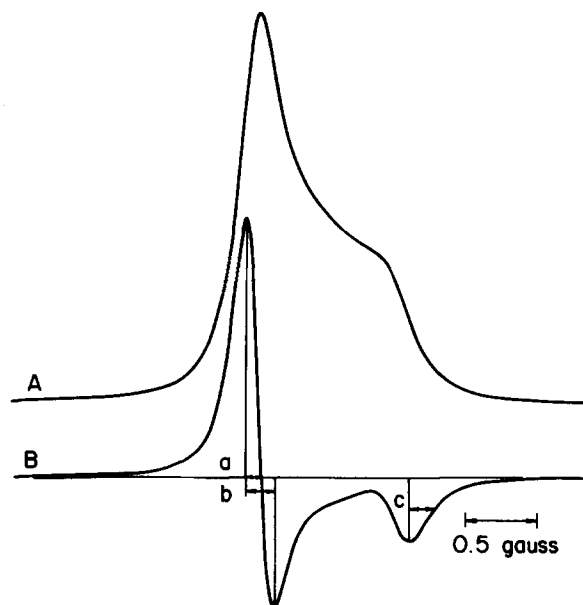


FIG. 4. Axially symmetric g -tensor cw absorption (A) and first derivative (B) spectra illustrating several linewidth definitions. Brownian diffusion, ($g_{\parallel} - g_{\perp} = -7.5 \times 10^{-4}$, $\tau_R = 1.0 \times 10^{-6}$ s, $|\mathcal{F}| \tau_R = 15$). First derivative peak-to-peak Lorentzian inhomogeneous linewidth = 0.1 G. (a) Maximum to zero crossing width; (b) peak-to-peak width; (c) outer half-width at half-height.

plotting $(\text{Re } \Lambda_1)^{-1}$ for $\tau_R > 3 \times 10^{-6}$ s.¹⁴

Our method then predicts a functional form of $T_M^e \propto \tau_R^b$ for the slow motional region, with $b \approx 1/2$, $2/3$, 1 for the Brownian, free and jump models, respectively. Thus we can write

$$T_M^e/\tau_R = C_1 |\mathcal{F} \tau_R|^{-1/2}, \quad \text{Brownian}, \quad (38)$$

$$T_M^e/\tau_R = C_2 |\mathcal{F} \tau_R|^{-1/3}, \quad \text{free } (Rt = 1), \quad (39)$$

$$T_M^e/\tau_R = C_3, \quad \text{jump } (Rt = 1), \quad (40)$$

where $\mathcal{F} \equiv \frac{2}{3}(\beta_0 H_0/\hbar)(g_{\parallel} - g_{\perp})$ and C_1 , C_2 , C_3 are constants. We have found $C_1 \approx 3$, $C_2 \approx 2$, and $C_3 \approx 1$. Note that $|\mathcal{F} \tau_R|$ is a dimensionless parameter that measures the extent to which the cw spectrum is characterized by slow tumbling. The larger the $|\mathcal{F} \tau_R|$, the closer is the spectrum to the rigid limit. Other workers have defined a T_M as the time it takes for the echo to decay to $1/e$ of its initial value (observed at about 200 ns). Figure 3 shows that these " T_M^e " results also depend upon the diffusion model with the exponents of τ_R for slow motion [cf. Eqs. (38)–(40), Table I], similar to but not

TABLE I. Values of b for g -tensor relaxation times: [relaxation time] $\propto \tau_R^b$.

Diffusion model	T_M^e ^a	T_M^e	Half-width at Half-height ^{b,d}	Peak-to-peak width ^{b,d}	Maximum to zero crossing width ^{b,d}
Brownian	0.43	0.34	0.53	0.63	0.63
Free ($Rt = 1.0$)	0.63	0.63	0.82	1.0	0.90
Jump ($Rt = 1.0$)	0.96 ^c	0.92	≥ 1.0	≥ 0.82	≥ 0.82

($g_{\parallel} - g_{\perp} = -7.5 \times 10^{-4}$).

^aCalculated by present method.

^b $\delta = 0.1$ G.

^c $T_M^e = (\text{Re } \Lambda_1)^{-1}$ for $\tau_R > 3 \times 10^{-6}$ s.

^dCf. Fig. 4.

identical to those for T_M^∞ . The discrepancies between the two methods is not surprising in view of the fact that the slow-motional envelopes are really a sum of decaying exponentials.

The different exponential dependence on $|\mathcal{F}\tau_R|$ for the different reorientational models is of some interest. The fact that for Brownian motion, slow motional spectra exhibit linewidths that go as $\tau_R^{-1/2}$ may be related to a result of Alexandrov *et al.*,¹⁵ who pointed out that the simple stochastic Liouville equation from a g tensor (or from a nitroxide in a simple "adiabatic" assumption) is of the form whose solutions are zero-order spheroidal wave functions of complex "potential." The real parts of the eigenvalues in the asymptotic limit of slow motion will all go as $(|\mathcal{F}|/\tau_R)^{1/2}$, although their coefficients (as well as their imaginary parts) will, in general, be different. Thus the $\tau_R^{-1/2}$ behavior of T_M^∞ appears as a natural consequence of the form of the differential equation for Brownian motion to which an angular dependent spin Hamiltonian is added. Baram¹⁶ has recently obtained a similar asymptotic result by another method.

In the case of jump diffusion for slow motions, one finds that, in general, the smallest eigenvalues are nearly identical in their real parts, differing only in their imaginary parts, and, of course, all these real parts exhibit a τ_R^{-1} dependence.

Some time ago, Mason and Freed¹⁷ offered an intuitive model for the τ_R dependence of cw linewidths in the slow motional region. They argued that in the near rigid limit, rotational jumps would carry the nitroxide radical between different orientations corresponding to substantially different ESR frequencies yielding an "uncertainty-in-lifetime broadening" given approximately by τ_R^{-1} . This is just the result of Eq. (40) for $(T_M^\infty)^{-1}$ for the jump model! Clearly, this is not the correct physical model for Brownian diffusion, where $(T_M^\infty)^{-1} \propto \tau_R^{-1/2}$. In Brownian diffusion, reorientation is by infinitesimal steps for which the spectral frequency change is also infinitesimal. Kivelson and Lee¹⁸ have recently suggested an approximate model that predicts the $\frac{1}{2}$ power law. In their model, one calculates the "motionally narrowed" linewidth (or T_2^{-1}) resulting from only the small ranges of angles (about a mean orientational angle) that the molecule can sample as a result of the slow reorientation. The range of angles sampled is determined by the "time scale" of the ESR experiment (*viz* T_2), so a greater range of angles is sampled the faster the motion. This appears to be a reasonable model in the Brownian limit. [For cw linewidths, discussed below, the presence of finite inhomogeneous broadening δ alters the results for Brownian motion, so that the exponent on τ_R approaches unity as δ increases. This might be explained by noting that for an observable effect, the Brownian motion must reorient the molecule out of the cone of angles from which each part of the ESR spectrum results, and the cones are increased in the presence of inhomogeneous broadening. These larger reorientations would then take on a character more like lifetime uncertainty broadening of the ESR spectrum as originally suggested by Mason and Freed.¹⁷]

Equations (38)–(40) show that estimates of τ_R may be

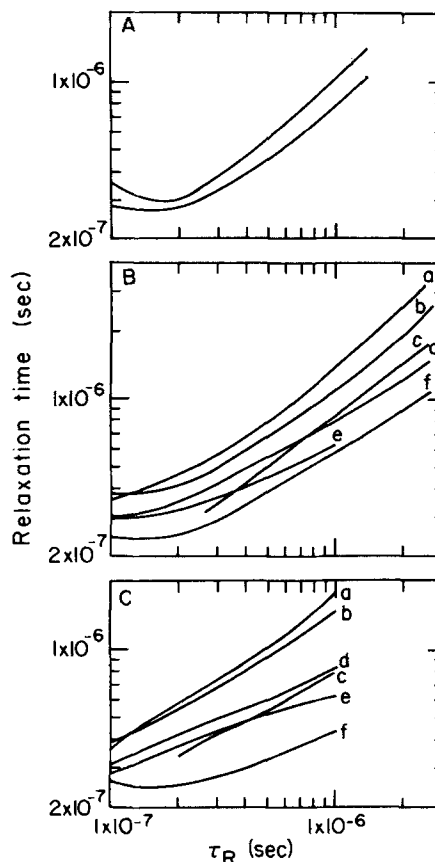


FIG. 5. Composite plots showing the relationships between various relaxation times. $(g_{\parallel} - g_{\perp}) = -7.5 \times 10^{-4}$. (A) jump diffusion, $Rt=1.0$; (B) free diffusion, $Rt=1.0$; (C) Brownian diffusion. (a) cw linewidth: $(2/3^{1/2})$ (peak-to-peak width) $^{-1}$; (b) cw linewidth: $3^{-1/2}$ (maximum to zero crossing width) $^{-1}$; (c) cw linewidth: (half-width at half-height) $^{-1}$; (d) T_M^∞ or $(\text{Re}\Delta_1)^{-1}$; (e) T_M^∞ from Stillman and Schwartz (Ref. 7); (f) T_M^∞ . (a)–(f) for jump diffusion all fall within the two solid lines in (A).

obtained from T_M^∞ (or from T_M^d), but one must have some idea of diffusion model. Estimates of τ_R can also be obtained from the cw spectrum, as is well known,^{9,17–19} and we wish to compare the simple approaches of treating the cw spectrum with the echo results.

Figure 4 shows typical absorption and derivative cw spectra for the axially symmetric g -tensor case, on which we have illustrated several definitions of linewidth. The linewidth of the high field derivative line is taken as the outer half-width at half-height minus the rigid limit value for the same quantity. The linewidth of the low field derivative line can be calculated in two ways: (1) peak-to-peak width multiplied by $(3)^{1/2}/2$ and (2) maximum-to-zero-crossing width multiplied by $(3)^{1/2}$. From each of these is subtracted the analogous rigid limit quantity. We simulated cw spectra using an inhomogeneous broadening contribution of $\delta = 0.1$ G and Lorentzian distribution.

Table I and Fig. 5 summarize the linewidth data along with all the previous data for each diffusion model. The τ_R exponents for the linewidths order as do the τ_R exponents for T_M^∞ , but in each case are slightly larger for the linewidth measurement. This result indicates the

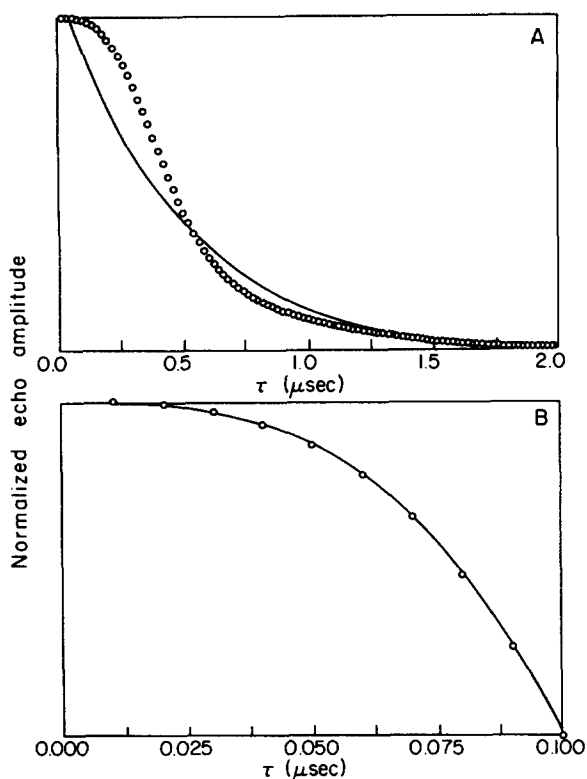


FIG. 6. A typical echo envelope showing short time $\exp(-c\tau^3)$ behavior Brownian diffusion, $(g_{\parallel} - g_{\perp}) = -7.5 \times 10^{-4}$, $\tau_R = 3.0 \times 10^{-6}$ s, $|\mathcal{F}| \tau_R = 44$. Circles—calculated points. (A) Solid line—best fit to $\exp(-2\tau/T_M)$, $T_M = 1.0 \times 10^{-6}$ s, (B) solid line—best fit to $\exp(-c\tau^n)$, $c = 6.1 \times 10^{18}$, $n = 2.97$.

distorting effect of the inhomogeneous broadening on the dependence of the cw widths on τ_R . The T_M^{∞} results do not include any inhomogeneous broadening, although they can be significantly affected (as can the cw widths) by other T_2 processes as the rotational motion slows sufficiently. We have found that as $\delta \rightarrow 0$, the τ_R exponents of the linewidths become more nearly equal to the T_M^{∞} results.

The estimates of T_M^{∞} described up until now have ignored the first 200 ns after the 180° pulse. Although this time period is as yet difficult to probe experimentally, it is easily studied theoretically, and Fig. 6 shows a typical echo decay as a function of τ for $0 < \tau < 2 \mu\text{s}$ and for $0 < \tau < 0.1 \mu\text{s}$. We have found that the initial portion of the $90^\circ\text{-}\tau\text{-}180^\circ\text{-}\tau$ decays can be fit almost exactly to the form $e^{-c\tau^3}$, a form reminiscent of that expected from translational diffusion in the presence of an inhomogeneous external magnetic field^{11,12,20}

$$M(2\tau) = M(0) \exp(-2\tau/T_2) \exp[-2(\gamma_e \partial H / \partial z)^2 D \tau^3 / 3]. \quad (41)$$

Our short time τ^3 fit is intuitively satisfying if in Eq. (41) we replace $\partial H / \partial z$, the linear inhomogeneity in the field with $|\mathcal{F}|$, a measure of the anisotropy of the spin Hamiltonian, and D , the translational diffusion coefficient, with τ_R^{-1} . Indeed, we have found that $c \cong 0.1 |\mathcal{F}|^2 \times \tau_R^{-1}$, independent of diffusion model. The short time τ^3 dependence of the echo envelope decay appears quite general. In fact, we are able to obtain its explicit form from a short time expansion of the stochastic Liouville equation for the case of Brownian motion. In particular,

we find that $c \cong \frac{1}{3} |\mathcal{F}|^2 \tau_R^{-1}$.

Our best fits of entire echo decays are based on fitting the initial portions to $\exp(-c\tau^3)$ and the final portions to $\exp(-d\tau)$, where $d \cong 2/T_M^{\infty}$. Examples are shown in Fig. 7. Note the intriguing difference between the echo envelope shape for the jump model, where the two forms appear to join together smoothly at a single τ , and that for the Brownian and free diffusion models, where the two forms hold only at the extremes of the echo envelope, with a large region in between. This model difference was found to hold for all cases tried. We expect that this range of τ where the cross over between the two forms takes place will contain important physical information. Also, note that a comparison of short-time vs long-time behavior can give information about the motional model, since the short time decay gives τ_R , while the long time decay depends also on the model.

2. Carr-Purcell sequences

Prompted by the close formal analogy between translation in an external inhomogeneous magnetic field and slow rotation of a molecule described by anisotropic magnetic parameters, we have calculated echo decays from a Carr-Purcell (CP) sequence using Eq. (34). Figure 8 shows three series of CP echo envelopes obtained for Brownian motion. Plotted with each series for comparison is the envelope from the simple $90^\circ\text{-}\tau\text{-}$

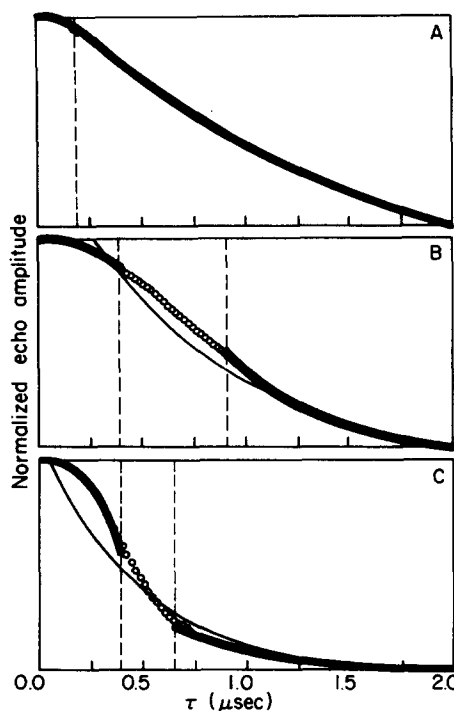


FIG. 7. Fit of echo envelopes (circles) to $N_1 \exp(-c\tau^3)$ (short times, heavy solid line) and to $N_2 \exp(2\tau/T_M^{\infty})$ (long times, heavy solid line). The thin solid line is the best fit of the entire envelope to $\exp(-2\tau/T_M)$. $(g_{\parallel} - g_{\perp}) = -7.5 \times 10^{-4}$. (A) Jump diffusion, $Rt = 1.0$, $\tau_R = 3.0 \times 10^{-6}$ s, $|\mathcal{F}| \tau_R = 44$, $N_1 = 1.0$, $c = 5.1 \times 10^{18}$, $N_2 = 1.1$, $T_M^{\infty} = 3.0 \times 10^{-6}$ s, $T_M = 2.9 \times 10^{-6}$ s; (B) free diffusion, $Rt = 1.0$, $\tau_R = 6.6 \times 10^{-6}$ s, $|\mathcal{F}| \tau_R = 96$, $N_1 = 1.0$, $c = 2.6 \times 10^{18}$, $N_2 = 3.0$, $T_M^{\infty} = 1.0 \times 10^{-6}$ s, $T_M = 1.5 \times 10^{-6}$ s; (C) Brownian diffusion, $\tau_R = 3.0 \times 10^{-6}$ s, $|\mathcal{F}| \tau_R = 44$, $N_1 = 1.0$, $c = 9.1 \times 10^{18}$, $N_2 = 0.8$, $T_M^{\infty} = 1.0 \times 10^{-6}$ s, $T_M = 9.9 \times 10^{-7}$ s.

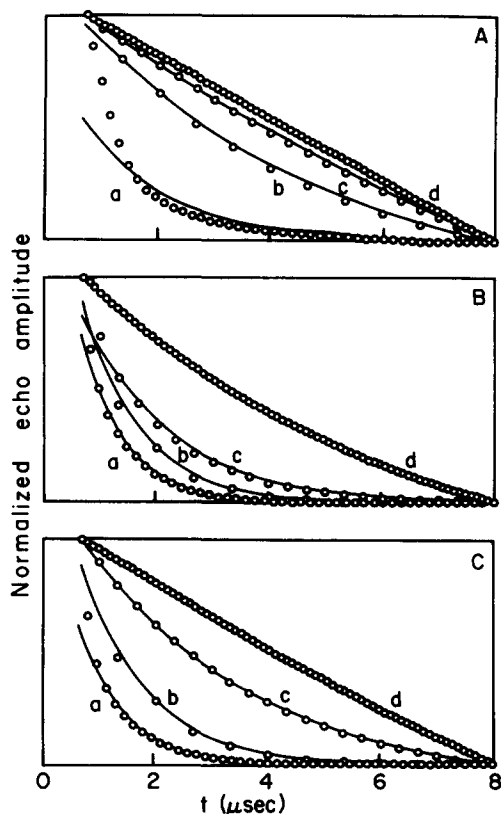


FIG. 8. Comparison of $90^\circ\text{-}\tau\text{-}180^\circ\text{-}\tau$ and Carr-Purcell (CP) echo envelopes (the alternating positive and negative signs in the CP envelope have been suppressed). Circles—calculated points, solid lines—best fit to $\exp(-2t/T_M^c)$ or to $\exp(-t/T_M^c)$. Brownian diffusion. (A) $(g_{||} - g_{\perp}) = -7.5 \times 10^{-4}$, $\tau_R = 5.0 \times 10^{-6}$ s, $|\mathcal{F}|\tau_R = 73$: (a) $90^\circ\text{-}\tau\text{-}180^\circ\text{-}\tau$, $T_M^c = 1.7 \times 10^{-6}$ s; (b) CP, $\tau = 0.32$ μ s, $T_M^c/T_M^{\infty} = 2.8$; (c) CP, $\tau = 0.16$ μ s, $T_M^c/T_M^{\infty} = 8.8$; (d) CP, $\tau = 0.05$ μ s, $T_M^c/T_M^{\infty} = 82$. (B) $(g_{||} - g_{\perp}) = -3.75 \times 10^3$, $\tau_R = 5.0 \times 10^{-6}$ s, $|\mathcal{F}|\tau_R = 360$: (a) $90^\circ\text{-}\tau\text{-}180^\circ\text{-}\tau$, $T_M^c = 7.6 \times 10^{-7}$ s; (b) CP, $\tau = 0.32$ μ s, $T_M^c/T_M^{\infty} = 1.3$; (c) CP, $\tau = 0.16$ μ s, $T_M^c/T_M^{\infty} = 2.1$; (d) CP, $\tau = 0.05$ μ s, $T_M^c/T_M^{\infty} = 9.1$. (C) $(g_{||} - g_{\perp}) = -7.5 \times 10^{-4}$, $\tau_R = 1.0 \times 10^{-6}$ s, $|\mathcal{F}|\tau_R = 15$: (a) $90^\circ\text{-}\tau\text{-}180^\circ\text{-}\tau$, $T_M^c = 8.2 \times 10^{-7}$ s; (b) CP, $\tau = 0.32$ μ s, $T_M^c/T_M^{\infty} = 1.3$; (c) CP, $\tau = 0.16$ μ s, $T_M^c/T_M^{\infty} = 3.7$; (d) CP, $\tau = 0.05$ μ s, $T_M^c/T_M^{\infty} = 35$.

$180^\circ\text{-}\tau$ sequence. The decays are normalized so that they all have the same value at the first point of the CP decay having the largest CP τ . It is seen that in each series, the $90^\circ\text{-}\tau\text{-}180^\circ\text{-}\tau$ envelope decays faster than any of the CP decays, which themselves decay slower and more like a single exponential the smaller the CP τ . We expect this qualitative behavior by analogy with the use of the CP sequence to remove the effect of translational diffusion in an inhomogeneous applied field. That is, an intuitive picture is that the successive 180° pulses repeatedly reverse the electron spin precession so rapidly that the g -tensor anisotropy is averaged more effectively than it can be randomized by the slow tumbling.

Figure 8(B) shows results for a case differing from that in Fig. 8(A) in that $|\mathcal{F}\tau_R|$ has been increased by increasing $|\mathcal{F}|$. As expected, a shorter CP τ is required to average the larger magnetic anisotropy, or, more precisely, to obtain the previous values of T_M^c/T_M^{∞} . (T_M^c

\equiv the phase memory time resulting from a CP sequence.) Note that except for CP τ 's so large and ineffective that $T_M^c \approx T_M$, the CP decay curves are either exponential or nearly exponential, so that while there is ambiguity in the definition of T_M for an ordinary $90^\circ\text{-}\tau\text{-}180^\circ\text{-}\tau$ echo (as discussed above), this is less true of T_M^c .

Figure 8(C) shows results from a case differing from that of Fig. 8(A) in that $|\mathcal{F}\tau_R|$ has been decreased by decreasing τ_R . Once again, shorter CP τ 's are required to obtain a previous T_M^c/T_M^{∞} ratio because a shorter τ is needed to scale to the shorter τ_R .

We have found that a natural way to plot the CP results is in terms of the dimensionless parameters T_M^c/T_M^{∞} vs τ_R/τ . Then, for each model, the results depend only on the product $|\mathcal{F}|\tau_R$. Plots for Brownian, free, and jump models are shown in Fig. 9. While all the curves are seen to (1) monotonically increase with τ_R/τ , and (2) be displaced to the right for larger $|\mathcal{F}|\tau_R$, we have, as yet, not found a simple functional form that approximates them.²¹ We note that these curves, while similar for the different models, nevertheless show some model-dependent differences. This suggests the possible use of CP sequences to study model dependence by experimentally running a series of CP sequences for different values of τ and comparing the results with theoretical calculations for different τ_R and model. (To facilitate the comparison, a plot of T_M^c/T_M^{∞} vs T_M/τ is most convenient since the axis variables are all experimental. Such a plot shows the same trends as that in Fig. 9.) The experiments should be repeated at several different temperatures, if possible, since the model-dependent differences do vary somewhat with $|\mathcal{F}|\tau_R$.

The main point that we wish to make is that such CP sequences are potentially more informative than just

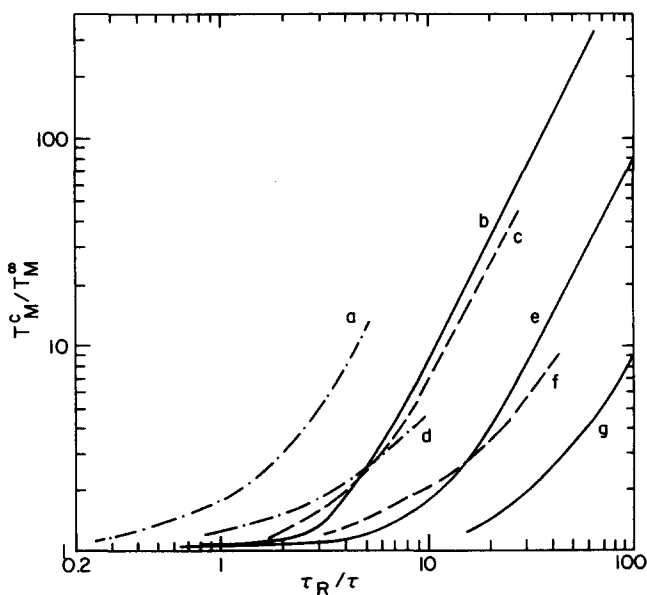


FIG. 9. Results of Carr-Purcell sequences. Solid lines—Brownian diffusion, dashed lines—free diffusion ($Rt=1.0$), dotted-dashed lines—jump diffusion ($Rt=1.0$). (a) $|\mathcal{F}|\tau_R = 5.8$; (b) $|\mathcal{F}|\tau_R = 15$; (c) $|\mathcal{F}|\tau_R = 19$; (d) $|\mathcal{F}|\tau_R = 20$; (e) $|\mathcal{F}|\tau_R = 73$; (f) $|\mathcal{F}|\tau_R = 96$; (g) $|\mathcal{F}|\tau_R = 360$.

simple two-pulse echoes. In the latter, usually only a single T_M (e. g., T_M^a) is obtained for a given sample at fixed experimental conditions, while in the former, a whole set of T_M^i are obtained vs τ , which could be used effectively to explore motional dynamics in greater detail.

Finally, we wish to call attention to the fundamental nature of CP sequences, viz. their ability to drive an otherwise irreversible process back toward reversibility, or more precisely, to cancel out the irreversibility, by the reversible averaging performed by the successive 180° pulses. One does not normally think of this as being possible in the fast motional limit where the echo appears totally determined by a single exponential decay for which $T_M = T_2$. However, we find that even in this limit, provided we study the full stochastic Liouville equation and use the full spectral-representation formula, then as long as $\tau \ll \tau_R$ and $\tau \lesssim |\mathcal{F}|^{-1}$, the irreversibility as manifested by a simple T_2 decay of the 90° - 180° echo is canceled out by the CP sequence. The main problem is an experimental one—to obtain CP pulses with short enough τ !

We conclude this section on simple g -tensor problems by noting that although the cases covered in this section (and the next) are restricted to those with axial magnetic parameters and isotropic reorientation, this restriction was done for convenience only and there is no fundamental reason limiting calculations to these limiting cases.

B. Axially symmetric nitroxide

We now consider the more complicated case of a nitroxide with two objectives: (1) One is typically able to irradiate only a portion of the ESR spectrum, so we use the nitroxide to illustrate the theory for partial irradiation and (2) nitroxides are an important class of spin probes and spin labels,⁹ so it is of value to have a quantitative basis for analyzing nitroxide echo experiments. In general, we find that most of the qualitative features we have already described for echoes from a g -tensor spectrum are also exhibited by nitroxides. We will discuss below special features of nitroxides.

A nitroxide spectrum has three hyperfine components and U is pure imaginary with three equal nonzero elements representing the coefficients of \mathcal{D}_{00}^0 in the expansions of the three allowed ESR transitions. Equations (31) and (33) become

$$\overline{s(2\tau)} \propto \text{Re} \sum_{j,i} a_{j,i} \exp(-[\Lambda_i + \Lambda_j^*]\tau), \quad (42)$$

$$a_{j,i} = \sum_{k=1}^3 \sum_i 0_{ki} 0_{kj}^* 0_{li} 0_{lj}^*. \quad (43)$$

Figure 10 shows typical cw absorption and derivative nitroxide spectra. The two outer extrema of the derivative spectra are quite characteristic, and several simple methods, based on the position and widths of the extrema relative to those in the rigid limit, have been developed for estimating τ_R directly from cw spectra.¹⁷⁻¹⁹ The extrema represent those nitroxide radicals whose $2p\pi$ orbital (on the nitrogen) is nearly parallel to the

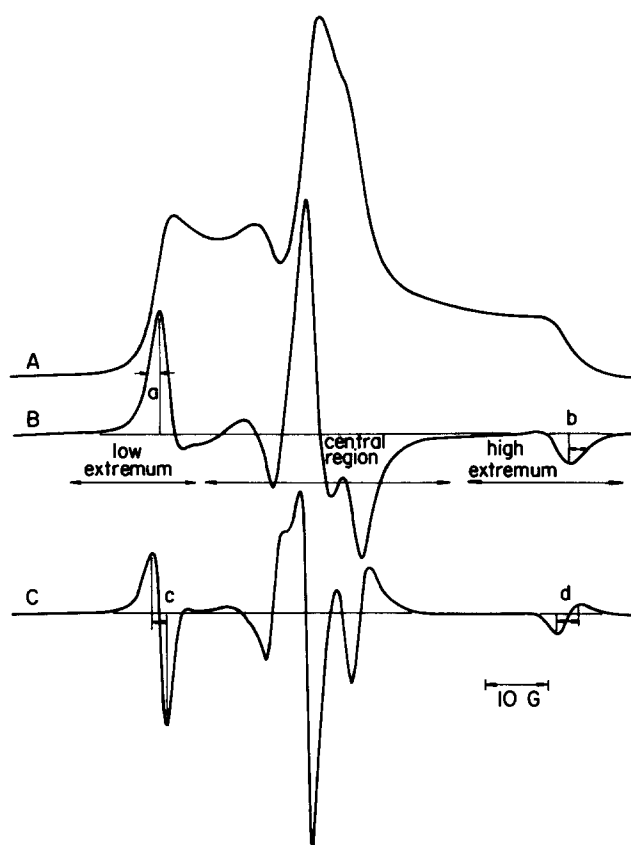


FIG. 10. cw absorption (A), first derivative (B) and second derivative (C) spectra illustrating several nitroxide linewidth definitions. Brownian diffusion, $(g_{\parallel} - g_{\perp}) = -6.0 \times 10^{-3}$, $(A_{\parallel} - A_{\perp}) = 29$ G, $\tau_R = 5.6 \times 10^{-8}$ s, $|\mathcal{F} + \mathcal{D}'|/\tau_R = 13$. First derivative peak-to-peak Lorentzian inhomogeneous linewidth = 1.0 G. (a), (b) first derivative outer half-width at half-height; (c), (d) second derivative peak-to-peak extrema widths.

applied field for either the $m_I = 1$ or $m_I = -1$ nuclear quantum states. Thus, isolating the nitroxide extrema is conceptually similar to isolating the "parallel" derivative peak in an axially symmetric g -tensor spectrum (e. g., the high field peak in Fig. 4).

Figure 11 shows the calculated T_M^a vs τ_R in the slow motional region for $200 \text{ ns} < \tau < 1.4 \mu\text{s}$ (typical experimental nitroxide studies⁵ would monitor τ up to $\sim 1 \mu\text{s}$). For each τ_R , T_M^a was calculated separately for the three regions of the cw spectrum: the two extrema ("low" and "high," cf. Fig. 10) and the central region. Thus, we are assuming that we can produce ideal pulses covering any of the three regions without affecting the other two, clearly an approximation.

As in the g -tensor case, these values of T_M^a are almost identical with $(\text{Re } \Lambda_1)^{-1}$ where now Λ_1 is the smallest eigenvalue of B which contributes to the region being "irradiated." We have plotted $(\text{Re } \Lambda_1)^{-1}$ instead of T_M^a for some of the points in Fig. 11(B) (free diffusion, $Rt = 1.0$) and for all of the points in Fig. 11(C) (jump model, $Rt = 1.0$).¹⁴ A fit of the data to the form $T_M^a \propto \tau_R^b$ gives the same b 's as were found in the g -tensor case: $\cong 1/2$, $\cong 2/3$, $\cong 1$ for Brownian, free ($Rt = 1.0$) and jump ($Rt = 1.0$) diffusion, respectively. There is some deviation

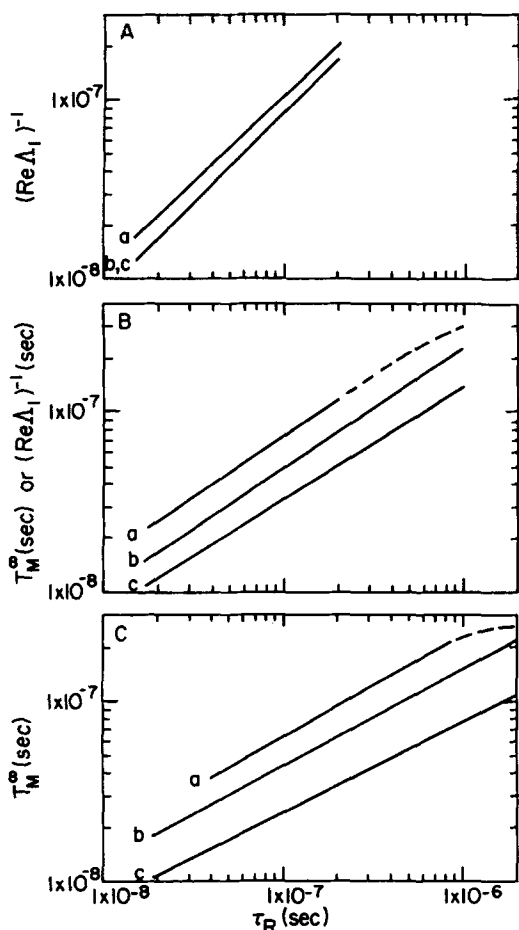


FIG. 11. Nitroxide phase memory times T_M^0 fit to $T_M^0 \propto \tau_R^b$. (A) jump diffusion, $Rt=1.0$ ($g_{||}-g_{\perp}$) = -4.8×10^{-3} , ($A_{||}-A_{\perp}$) = 30 G: (a) central region, $b \approx 0.95$; (b), (c) low, high extrema, $b \approx 0.97$. (B) free diffusion, $Rt=1.0$ ($g_{||}-g_{\perp}$) = -6.0×10^{-3} , ($A_{||}-A_{\perp}$) = 29 G, $(\text{Re } \Delta_1)^{-1}$ is plotted for $\tau_R > 3 \times 10^{-7}$ s: (a) central region, $b \approx 0.67$; (b) low extremum, $b \approx 0.67$; (c) high extremum, $b \approx 0.63$. (C) Brownian diffusion, ($g_{||}-g_{\perp}$) = -6.0×10^{-3} , ($A_{||}-A_{\perp}$) = 29 G: (a) central region, $b \approx 0.56$; (b) low extremum, $b \approx 0.54$; (c) high extremum, $b \approx 0.50$.

for the central region (large τ_R 's) when the smallest eigenvalue is plotted instead of the calculated T_M^0 . This deviation is probably due to the fact that there are so many contributing eigenvalues of similar magnitude to the central part of the near rigid-limit spectrum that a single eigenvalue decay constant is not valid except for unreasonably long time intervals.

These results imply slow motional equations of the form

$$T_M/\tau_R \approx C_1(\tau_R |\mathcal{F} + \mathcal{D}'|)^{-1/2}, \quad \text{Brownian}, \quad (44)$$

$$T_M/\tau_R \approx C_2(\tau_R |\mathcal{F} + \mathcal{D}'|)^{-1/3}, \quad \text{free } (Rt=1), \quad (45)$$

$$T_M/\tau_R \approx C_3, \quad \text{jump } (Rt=1), \quad (46)$$

where C_1 , C_2 , C_3 are dimensionless constants and $\mathcal{D}' \equiv \frac{2}{3}(A_{||}-A_{\perp})$, cf. Eqs. (38)–(40). We have found $C_1 \approx 2, 3.5, 1$; $C_2 \approx 1, 2, 1$; and $C_3 \approx 0.9, 1.4, 0.9$ for the low extremum, central region and high extremum, respectively.

We show in Fig. 12 experimental data, previously re-

ported,⁵ from a spin echo study of Tempone in 85% glycerol/15% water solvent. The superimposed lines are plots of $(\text{Re } \Delta_1)^{-1}$ from the central region of the spectrum for the jump model ($Rt=1.0$) and free diffusion model ($Rt=1.0$).²³ A separate cw study²⁴ (using the perdeuterated solute and glycerol- d_3 /D $_2$ O solvent) established the relationship between τ_R and temperature for the jump and free $Rt=1.0$ models which we use here to plot our eigenvalue results (calculated as a function of τ_R) against temperature, namely,

$$\ln \tau_R/\tau_{R0} = E_A/RT, \quad (47)$$

where $E_A = 15$ kcal/mol and $\tau_{R0} = 2.3 \times 10^{-21}$ s.

In the fast motional region, the experimental echo T_M 's, the calculated $(\text{Re } \Delta_1)^{-1}$'s and the experimental T_2 's obtained from the cw study (not shown in the figure) agree quite well. In particular, the cw T_2 's (which cover the range 5×10^{-8} s $\leq T_2 \leq 6 \times 10^{-7}$ s) and the $(\text{Re } \Delta_1)^{-1}$'s match perfectly.

In the model dependent slow motional region, we find

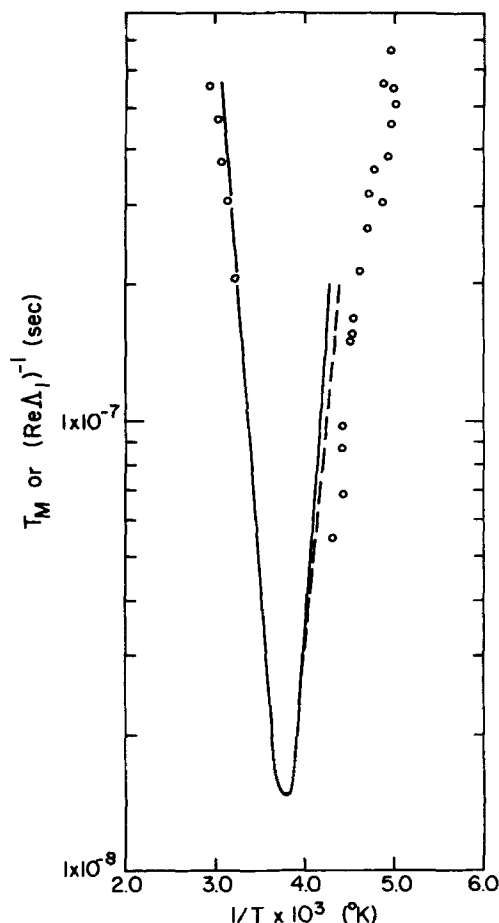


FIG. 12. Superposition of central region $(\text{Re } \Delta_1)^{-1}$ values onto a plot of experimental T_M values obtained from a study (Ref. 5) of Tempone/85% glycerol–15% water. Open circles—experimental points, solid line—jump diffusion ($Rt=1.0$), dashed line—free diffusion ($Rt=1.0$). Actual magnetic parameters (Ref. 24) are $g_x, g_y, g_z = 2.0084, 2.0060, 2.0022$ and $A_x, A_y, A_z = 5.5, 5.7, 35.8$ G. The calculations used axial approximations (Ref. 23): $g_x = g_y = 2.0075, g_z = 2.0027$ and $A_x = A_y = 6.0$ G, $A_z = 36.0$ G.

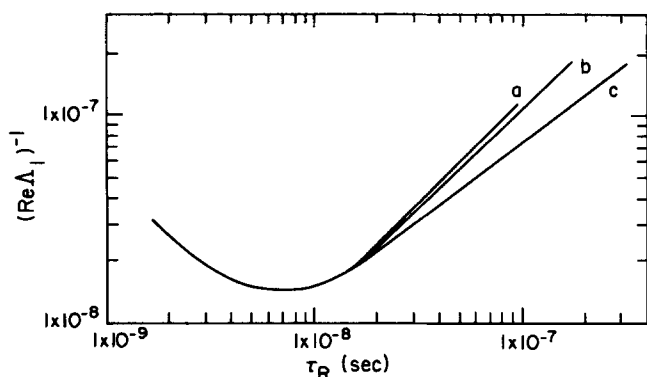


FIG. 13. Central region $(\text{Re } \Lambda_1)^{-1}$ values for jump diffusion. The curves can be fit, for large τ_R , as $(\text{Re } \Lambda_1)^{-1} \propto \tau_R^b$. $(g_{\parallel} - g_{\perp}) = -4.8 \times 10^{-3}$, $(A_{\parallel} - A_{\perp}) = 30$ G: (a) $Rt = 10$, $b \approx 0.89$; (b) $Rt = 1.0$, $b \approx 0.96$; (c) $Rt = 0.1$, $b \approx 0.73$.

that the $(\text{Re } \Lambda_1)^{-1}$ lines do not match the experimental spin echo T_M points. The jump $(\text{Re } \Lambda_1)^{-1}$, as shown above, follow the relationship $(\text{Re } \Lambda_1)^{-1} \approx T_M^{\infty} \approx \tau_R$; the experimental T_M 's follow $T_M \approx \tau_R/6$. The free diffusion line veers more toward the experimental points, but with the wrong slope. We note here that the previous cw simulations were not sensitive enough to distinguish between jump and free model fits, and the Brownian model did not fit the cw data well.

Figure 13 shows results of additional jump calculations with $Rt = 0.1$ (weak jump) and $Rt = 10$ (strong jump). They show that while $Rt = 1.0$ is already close to the strong jump limit, $Rt = 0.1$ gives a $(\text{Re } \Lambda_1)^{-1} \tau_R^b$ dependence with b less than 1, a trend closer to that of the free diffusion model. There is the possibility of a better fit, therefore, in Fig. 12²⁵ if other models and Rt values are explored. Even from the $Rt = 1.0$ points already

plotted in Fig. 12, however, it is clear that the echo theory that we are using, and indeed the T_M^{∞} limit [i. e., $T_M \approx T_M^{\infty} \approx (\text{Re } \Lambda_1)^{-1}$] that we are assuming here, contains most of the important features of real systems. Further comparisons of this kind require careful *combined* experimental cw studies and spin echo studies on the same sample and such work is in progress.

Nitroxide slow motional extrema linewidth results are summarized in Table II. We have calculated the motional width by following Mason *et al.*¹⁹ who measure the outer half-width at half-height linewidths of the two individual extrema minus the effective widths of the rigid limit extrema, and Kivelson and Lee,¹⁸ who measure the difference between the peak-to-peak linewidths of the two extrema. In effect, the method of Mason *et al.*^{17,19} uses the widths of the two extrema to extract both τ_R and the *effective* inhomogeneous width. The method of Kivelson and Lee¹⁸ attempts to cancel out the role of the latter by taking differences. We have calculated these quantities from both the first and second derivative spectra and are particularly interested in the role of the inhomogeneous linewidth.

We find the following trends. When the superimposed inhomogeneous linewidth is small (e. g., 0.1 G, compared to a nitroxide spectrum of extent ~ 100 G), all of the above methods give the same value for Brownian diffusion for b in the equation (inverse linewidth) = $a\tau_R^b$: $b \approx \frac{1}{2}$, while a is method dependent, as shown in Table II. As the inhomogeneous linewidth is increased to realistic values, however, both a and b increase, with the second derivative results increasing somewhat more smoothly^{18,26} than those from the first derivative spectra. The conclusion is that the inhomogeneous broadening due to nonmotional causes can have important effects on the spectra. The first method^{17,19} thus requires fitting data by interpolating from Table II, while the second method¹⁸

TABLE II. Nitroxide linewidth data, Brownian diffusion: $(\text{linewidth})^{-1} = a\tau_R^b$.

δ^d	Low extremum ^a				High extremum ^b			
	0.1	1	3	5	0.1	1	3	5
b^e	0.45	0.81	0.85	0.46	0.46	0.67	0.71	0.98
$a^{e,g}$	7.7×10^{-5}	4.1×10^{-2}	1.0×10^{-1}	2.5×10^{-4}	5.2×10^{-5}	2.0×10^{-3}	4.5×10^{-3}	5.6×10^{-1}
b^f	0.48	0.81	1.1	1.1	0.47	0.64	1.2	1.0
$a^{f,g}$	1.1×10^{-4}	3.2×10^{-2}	8.7	3.9	5.3×10^{-5}	1.0×10^{-3}	5.9	8.4×10^{-1}
Extrema difference ^c								
δ^d	0.1	1	3	5				
b^e	0.46	0.57	0.50	0.27				
$a^{e,g}$	1.3×10^{-4}	7.8×10^{-4}	2.4×10^{-4}	4.8×10^{-6}				
b^f	0.46	0.52	0.65	0.68				
$a^{f,g}$	1.1×10^{-4}	2.7×10^{-4}	3.4×10^{-3}	5.6×10^{-3}				

$(g_{\parallel} - g_{\perp}) = -6.0 \times 10^{-3}$, $(A_{\parallel} - A_{\perp}) = 29$ G.

^aLow extremum linewidth minus rigid limit low extremum linewidth.

^bHigh extremum linewidth minus rigid limit high extremum linewidth.

^cHigh extremum linewidth minus low extremum linewidth.

^dFirst derivative peak-to-peak Lorentzian inhomogeneous line broadening G.

^eFirst derivative outer half-width at half-height $\times 2(3)^{-1/2}$, cf. Fig. 10.

^fSecond derivative peak-to-peak linewidth G, cf. Fig. 10.

^g a is in units of $[s]^{1-b}$.

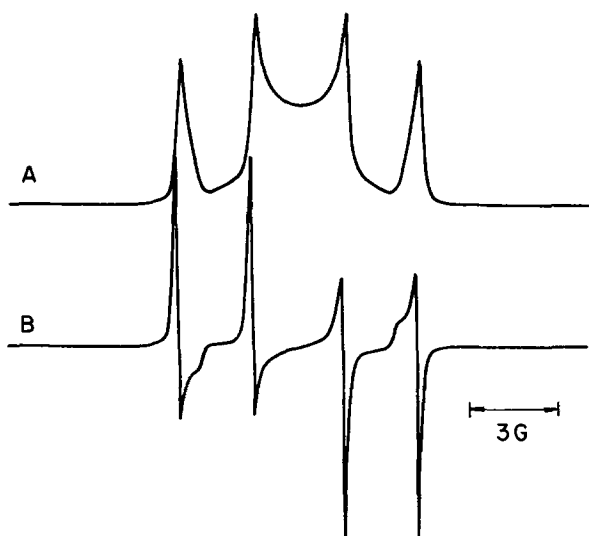


FIG. 14. cw absorption (A) and first derivative (B) spectra for the case $I=1/2$, $g_e=2.002$, $A_x=A_y=-3.25$ G, $A_z=6.5$ G, $g_n=5.5854$, Brownian diffusion, $\tau_R=3.6 \times 10^{-9}$ s, $H_0=2200$ G showing the two allowed and two forbidden transitions. The first derivative peak-to-peak Lorentzian inhomogeneous linewidth is 0.1 G.

still requires correction for effects of inhomogeneous broadening that are not subtracted out. In comparison, echo T_M^∞ results are not affected by inhomogeneous broadening although they would be affected by additional T_2 (relaxation) processes that are independent of the radical tumbling. These latter processes are typically much smaller in magnitude than the inhomogeneous broadening due to proton (or deuteron) superhyperfine structure which affects nitroxide radicals.

C. Nuclear modulation

For cases where there is an electron-nuclear hyperfine interaction, and the hyperfine field seen by the nucleus is comparable in magnitude to the external field, the nuclear spin can be quantized along a different axis than the electron spin. As the external pulsing sequence reorients the electron spin, the changing hyperfine field at the nucleus can cause it to reorient as well, resulting in a "forbidden transition" where both spins flip simultaneously. The coherent precessing field due to the nucleus then modulates the external field felt by the electron, and this modulation is seen in the electron echo envelope. The depth and frequencies of the modulation structure for rigid limit patterns have been analyzed to gain information about the kind of nuclei present, their number, distance from the electron site and arrangement.^{27,28}

In order to produce nuclear modulation in the simulations, one must retain the nuclear Zeeman term in the Hamiltonian (it was safely omitted in the nitroxide simulations of Sec. B). Equations (31) and (33) are applicable for this case provided we use the more general interpretation of the asterisk (i. e., complex conjugate of all terms of A_{ij} in \hat{S} , with the nuclear Zeeman term unchanged). Thus Λ_i , 0_{ij} are the eigenvalues and eigenvectors of B calculated using $\hat{\mathcal{H}}(\Omega)$ from Eqs. (2),

(3), and (4), while Λ_j^* , 0_{ij}^* are the eigenvalues and eigenvectors of B calculated from $\hat{\mathcal{H}}'(\Omega)$, where $\hat{\mathcal{H}}'(\Omega)$ is identical to $\hat{\mathcal{H}}(\Omega)$ except that $\omega_n \rightarrow -\omega_n$, where $\omega_n = -\gamma_n H_0$. This means that two separate diagonalizations are required.

Figure 14 shows a close to rigid limit powder cw spectrum for the case $I=\frac{1}{2}$. The nuclear hyperfine tensor elements and nuclear gyromagnetic ratio are appropriate for an "ideal" hydrogen atom located ~ 3.8 Å from the electron (calculated assuming a point dipole approximation, an axially symmetric hyperfine interaction and no isotropic hyperfine interaction). The external field was chosen to equalize the intensity of the two allowed vs that of the two forbidden transitions, a situation which maximizes the echo modulation depth.²⁸ The intensities of the two types of transitions are equal for²⁹

$$\frac{H}{A_{zz}} \cong \frac{h}{2g_n\beta_n}, \quad (48)$$

where A_{zz} is the principle axis value of the nuclear hyperfine tensor. Figure 15 shows the rigid limit powder echo envelope expected from the parameters used in creating Fig. 14. This envelope was calculated from the following well known equations which were then isotropically averaged over θ ²⁷:

Modulation amplitude (2τ)

$$= 1 - 2k \sin^2\left(\frac{\omega_\alpha \tau}{2}\right) \sin^2\left(\frac{\omega_\beta \tau}{2}\right), \quad (49)$$

with

$$k = \left(\frac{\omega_I B}{\omega_\alpha \omega_\beta}\right)^2, \quad (50a)$$

$$\omega_I = (g_n \beta_n H_0)/\hbar, \quad (50b)$$

$$\omega_\alpha = \left[\left(\frac{A}{2} + \omega_I\right)^2 + \left(\frac{B}{2}\right)^2\right]^{1/2}, \quad (50c)$$

$$\omega_\beta = \left[\left(\frac{A}{2} - \omega_I\right)^2 + \left(\frac{B}{2}\right)^2\right]^{1/2}, \quad (50d)$$

$$A = \frac{1}{\hbar} \frac{g_e g_n \beta_e \beta_n}{r^3} (3 \cos^2 \theta - 1) + 2\pi a, \quad (50e)$$

$$B = \frac{1}{\hbar} \frac{g_e g_n \beta_e \beta_n}{r^3} (3 \cos \theta \sin \theta). \quad (50f)$$

Figure 16 is a series of echo envelopes for Brownian diffusion, calculated by our method, showing how the modulation structure is averaged by the random radical motions. Note that these envelopes cannot be reproduced by merely multiplying the rigid limit pattern in Fig. 15 by a decay term $\exp(-2\tau/T_M)$.

The motionally averaged nuclear modulation patterns were found to be much more sensitive to their method of calculation than are the echoes discussed previously. Often, the modulated echoes require a larger basis set [cf. Eq. (23)] for convergence than is necessary for the corresponding cw spectrum, whereas for the unmodulated echoes, the same basis set can be used for both calculations. Furthermore, too large a basis set can also change the modulation results, leading to a pattern

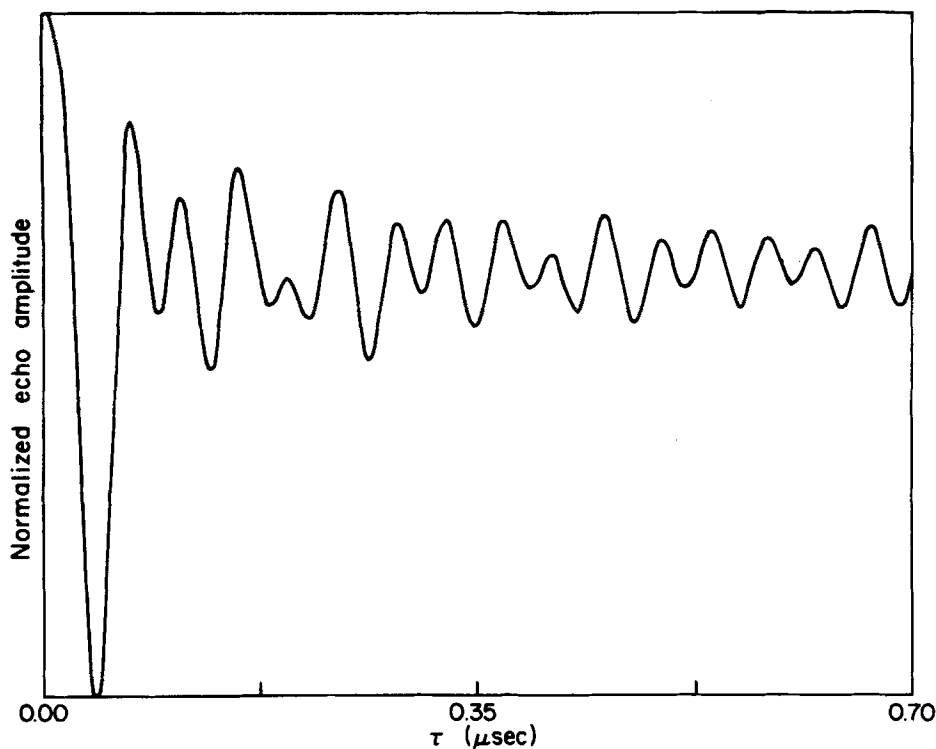


FIG. 15. Rigid limit powder echo envelope expected from the parameters given in Fig. 14.

with less structure. This sensitivity of the modulation calculation is not surprising since not only does it depend on small differences in the imaginary parts of the eigenvalues of B [cf. Eq. (31)], but it depends further on small differences between the eigenvalues of B calculated from $\hat{\mathcal{H}}(\Omega)$ and those calculated from $\hat{\mathcal{H}}'(\Omega)$, as explained earlier in this section.

In order to obtain as accurate a set of eigenvalues for the modulation patterns as possible, we used the Rutishauser tridiagonalizing routine as the first step in the diagonalization of the two B matrices.¹⁰ Although the Rutishauser algorithm is a more time consuming algorithm than is the Lanczos algorithm [which was used (and found to be completely reliable) in calculating all the cw spectra and echoes discussed in Sec. B], the Rutishauser algorithm is known to be more accurate.¹⁰ The above mentioned convergence complications were present even with the Rutishauser algorithm, however, and the slow "beat" present in Fig. 16(A) may be due to slight inaccuracies in the eigenvalues.

As was previously done, modulation patterns may also be calculated for the free and jump diffusion models. These patterns look similar to those calculated for the Brownian model.

III. SUMMARY

We have shown how spectral methods in terms of the eigenvalues and eigenfunctions of the stochastic Liouville operator permit a convenient representation of echo pulse sequences, and permit their accurate computation in slow motional problems. In general, the echo decay is given by a sum of exponentials of complex argument whose real coefficients of time give the damp-

ing and whose imaginary parts can give oscillations.

It is particularly convenient for computation to regard the microwave pulses as ideal, i. e., of exactly 90° or 180° and of infinitesimal duration, although it is possible to extend these methods to diagonalizing the stochastic Liouville operator in the presence of all terms including the microwave radiation term. Our calculations for ideal pulses compare very favorably with a previous

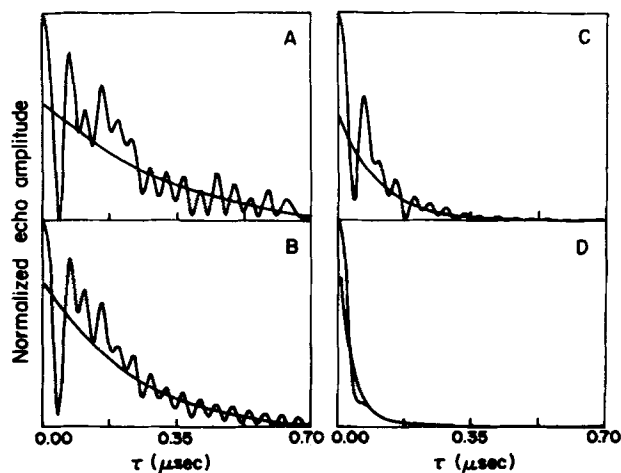


FIG. 16. Series of echo envelopes for Brownian diffusion showing the effects of motional averaging on the nuclear modulation pattern. Superimposed are the best fits to $\exp(-2\tau/T_M)$. Parameters are those given in Fig. 14, except: (A) $\tau_R = 3.6 \times 10^{-5}$ s, $T_M = 7.5 \times 10^{-7}$ s; (B) $\tau_R = 3.6 \times 10^{-6}$ s, $T_M = 4.8 \times 10^{-7}$ s; (C) $\tau_R = 3.6 \times 10^{-7}$ s, $T_M = 2.1 \times 10^{-7}$ s; (D) $\tau_R = 3.6 \times 10^{-8}$ s, $T_M = 7.6 \times 10^{-8}$ s.

complete calculation done for a simple g -tensor case but in the presence of a finite radiation field of finite duration.⁷ A useful feature of the method presented here, aside from computational convenience, is that the eigenvalues and eigenfunctions of the stochastic Liouville operator in the absence of radiation may be used to calculate both the echo signal and also the cw spectrum. The method also emphasizes the different manner in which echoes probe motional details vs the cw motional dependence.

We have shown by means of some prototype examples how the echo phase memory time T_M^∞ may be used to measure slow motion rotational correlation times τ_R (for isotropic motion). We obtain the interesting result that $T_M^\infty \propto \tau_R^b$ where the exponent b depends on the model of reorientation ($b = \frac{1}{2}$ for Brownian motion to $b = 1$ for jump diffusion). We have illustrated, with some recent results on a nitroxide probe,⁵ how one may use these T_M^∞ in conjunction with analysis of slow motional cw spectra to study motional dynamics in greater detail than can be studied with either method separately.

As the time resolution of ESE spectrometers is improved, one may hope to study echoes after short τ . Our theoretical analysis leads to a short-time behavior of the echoes that goes as $\exp(-c\tau^3)$, where $c \cong \mathcal{F}^2/9\tau_R$ for all the models considered, but the cross-over region to the longer time $\exp(-2\tau/T_M^\infty)$ behavior appears to be very model dependent, and worthy of further study. We also found that in all cases $T_M^\infty \cong (\text{Re } \Lambda_1)^{-1}$, where Λ_1 is the slowest decaying eigenvalue, as one might expect.

The formal analogy between the $\exp(-c\tau^3)$ short time behavior of the slow-motional echoes and the well-known exponential in τ^3 behavior for echoes from translational diffusion in an inhomogeneous field led us to consider Carr-Purcell sequences and slow motion, especially since CP sequences are now becoming feasible on ESE spectrometers.³⁰ Indeed we find that rapid sets of 180° pulses which reverse the electron-spin precession can effectively average out the anisotropy in the spin Hamiltonian, but this does require $\tau \ll \tau_R$ plus $\tau \leq |\mathcal{F}|^{-1}$ for g tensors or $\tau \leq [\mathcal{D}' + \mathcal{F}]^{-1}$ for nitroxides. In this limit, the (nearly) exponential decay of the CP envelope T_M^c becomes much greater than T_M^∞ . One can study this effect as a function of τ from large τ where $T_M^c \cong T_M^\infty$ to the shorter τ limit. In particular, we obtain universal curves for graphs of T_M^c/T_M^∞ vs τ_R/τ which only depend on $|\mathcal{F}|\tau_R$ and model. We have discussed how such graphs provide more information on motional dynamics and diffusion model than do simple echo sequences. We note that some recent preliminary experiments are consistent with the predicted trends.³⁰

As another example of the application of our method, we have studied echo modulation patterns, which arise, for example, for weakly coupled protons (or deuterons) with substantial nuclear Larmor frequencies and anisotropic hyperfine interactions. These are effectively predicted by diagonalizing two nearly identical stochastic Liouville operators (they differ only in sign of the nuclear Zeeman term). We are able to study how the rotational motion averages out these modulation patterns

as it speeds up. We find that the motional effects cannot be accurately represented merely by multiplying the pattern expected for the rigid limit by a single exponential decay. This is as expected in view of the fact that the echo envelope is again representable as a sum of exponentials, with, in general, different decays. We conclude that studies of motional effects on echo modulation patterns should be sensitive to very slow motions $\tau_R \sim \mathcal{D}'^{-1}$, where \mathcal{D}' measures the magnitude of the anisotropic proton hyperfine interaction. This could be of considerable importance in extending the range of ESE to slower motions.

Clearly the method described here, as well as the general theory on which it is based,^{7,8} may be applied to a variety of pulse sequences both for ESE and for nuclear spin echoes to explore and study their utility for experiments on slow motions.

ACKNOWLEDGMENT

We wish to acknowledge with pleasure helpful conversations and advice from Dr. Giorgio Moro relating to the computational aspects of this work.

- ¹K. M. Salikov, A. G. Semenov, and Yu. D. Tsvetkov, *Electron Spin Echoes and Their Applications* (Nauka, Novosibirsk, 1976).
- ²*Time Domain Electron Spin Resonance*, edited by L. Kevan and R. N. Schwartz (Wiley-Interscience, New York, 1979).
- ³A. E. Stillman and R. N. Schwartz, *J. Phys. Chem.* **85**, 3031 (1981).
- ⁴I. M. Brown, *J. Chem. Phys.* **60**, 4930 (1974); I. M. Brown, in *Time Domain Electron Spin Resonance*, edited by L. Kevan and R. N. Schwartz (Wiley-Interscience, New York, 1979), Chap. 6.
- ⁵A. E. Stillman, L. J. Schwartz, and J. H. Freed, *J. Chem. Phys.* **73**, 3502 (1980); **76**, 5658 (1982).
- ⁶L. J. Schwartz, M. Shiotani, and J. H. Freed (to be published).
- ⁷A. E. Stillman and R. N. Schwartz, *J. Chem. Phys.* **69**, 3532 (1978); A. E. Stillman and R. N. Schwartz, in *Time Domain Electron Spin Resonance*, edited by L. Kevan and R. N. Schwartz (Wiley-Interscience, New York, 1979), Chap. 5.
- ⁸J. H. Freed, *J. Phys. Chem.* **78**, 1155 (1974); J. H. Freed in *Time Domain Electron Spin Resonance*, edited by L. Kevan and R. N. Schwartz (Wiley-Interscience, New York, 1979), Chap. 2.
- ⁹J. H. Freed, in *Spin Labelling Theory and Applications*, edited by L. J. Berliner (Academic, New York, 1976), Chap. 3.
- ¹⁰G. Moro and J. H. Freed, *J. Chem. Phys.* **74**, 3757 (1981).
- ¹¹C. P. Slichter, *Principles of Magnetic Resonance* (Springer, New York, 1980).
- ¹²A. Abragam, *The Principles of Nuclear Magnetism* (Oxford University, London, 1961).
- ¹³G. V. Bruno, Ph.D. thesis, Cornell University, Ithaca, New York, 1973.
- ¹⁴Convergence in the calculation requires larger basis sets [cf. Eq. (23)] as one progresses from Brownian to free to jump diffusion models.
- ¹⁵I. V. Alexandrov, A. N. Ivanova, N. N. Korst, A. V. Lazarev, A. I. Prikhozhenko, and V. B. Stryukov, *Mol. Phys.* **18**, 681 (1970).
- ¹⁶A. Baram, *Mol. Phys.* **44**, 1009 (1981).
- ¹⁷R. P. Mason and J. H. Freed, *J. Phys. Chem.* **78**, 1321 (1974).

- ¹⁸D. Kivelson and S. Lee, *J. Chem. Phys.* **76**, 5746 (1982).
- ¹⁹R. P. Mason, E. B. Giavedoni, and A. P. Dalmasso, *Biochemistry* **16**, 1196 (1977).
- ²⁰G. P. Zientara and J. H. Freed [*J. Chem. Phys.* **72**, 1285 (1980)] have used numerical methods to integrate the stochastic Liouville equation for the problem of spin echoes for translational diffusion in bounded heterogeneous media.
- ²¹Preliminary attempts to fit the curves in Fig. 9 show that they rise more steeply than a simple power law $\alpha(\tau_R/\tau)^n$ but more slowly than an exponential of the form $\exp(a\tau_R/\tau)$.
- ²²*Spin Labeling Theory and Applications*, edited by L. J. Berliner (Academic, New York, 1976), Vol. 1, Vol. 2 (1979).
- ²³For convenience, the $(\text{Re } \Lambda_1)^{-1}$ were calculated assuming axially symmetric magnetic parameters (cf. figure caption, Fig. 12). $(\text{Re } \Lambda_1)^{-1}$ calculated using the jump diffusion model is independent of the A and g tensors [cf. Eq. (46)], while the free diffusion model gives results for the central region which are insensitive to small changes in the g -tensor values.
- ²⁴J. S. Hwang, R. P. Mason, L. P. Hwang, and J. H. Freed, *J. Phys. Chem.* **79**, 489 (1975).
- ²⁵In order to fit computer results to experimental data, one needs a relationship between temperature (the experimental variable) and τ_R (the theoretical variable). The previous cw study (Ref. 24) obtained such a relationship only for the approximate free ($Rt=10$) and jump ($Rt=1.0$) diffusion models. Further fitting of the results of echo calculations depends on obtaining T - τ_R relationships for other models and Rt values and such work is in progress.
- ²⁶S. Lee, *Phys. Rev. B* **23**, 6151 (1981).
- ²⁷L. Kevan, in *Time Domain Electron Spin Resonance*, edited by L. Kevan and R. N. Schwartz (Wiley-Interscience, New York, 1979), Chap. 8.
- ²⁸W. B. Mims, in *Electron Paramagnetic Resonances*, edited by S. Geschwind (Plenum, New York, 1972), Chap. 4.
- ²⁹I. Miyagawa and W. Gordy, *J. Chem. Phys.* **32**, 255 (1960).
- ³⁰U. Eliav, Cornell University (work in progress).